Soft Matter

Multi-scale Progressive Failure Mechanism and Mechanical Properties of Nanofibrous Polyurea Aerogels

Journal:	*Soft Matter*
Manuscript ID	SM-ART-07-2018-001546.R1
Article Type:	Paper
Date Submitted by the Author:	21-Aug-2018

Complete List of Authors:	Wu, Chenglin; Missouri University of Science and Technology, Civil, Architectural, and Environmental Engineering Taghvaee, Tahereh; Missouri University of Sci & Techn, Chemistry Wei, Congjie; Missouri University of Science and Technology, Civil, Architectural, and Environmental Engineering Ghasemi, Arman; The University of Texas at San Antonio, Mechanical Engineering Chen, Genda; Missouri University of Science and Technology, Civil, Architectural, and Environmental Engineering Leventis, Nicholas; Missouri University of Sci & Techn, Chemistry Gao, Wei; The University of Texas at San Antonio, Mechanical Engineering

Multi-scale Progressive Failure Mechanism and Mechanical Properties of Nanofibrous Polyurea Aerogels

Chenglin Wu,[a*], Tahereh Taghvaee [b], Congjie Wei [a], Arman Ghasemi [c], Genda Chen [a], Nicholas Leventis [b], Wei Gao [c]

[a] Department of Civil, Architectural, and Environmental Engineering, Missouri University of Science and Technology, Rolla, MO 65401,

[b] Department of Chemistry, Missouri University of Science and Technology, Rolla, MO 65401

[c] Department of Mechanical Engineering, The University of Texas at San Antonio, San Antonio, TX, 78249, United States

*Corresponding Author, Email: wuch@mst.edu

Submitted to
Soft Matter
April 2018

Abstract

The nonlinear mechanical properties, deformation and failure mechanisms of polyurea aerogels (PUAs) were investigated using a multi-scale approach that combines nanoindentation, analytical and computational modeling. The atomistic structure of primary particles of PUAs and their mechanical interactions were investigated with molecular dynamics simulations. From nanoindentation we identified four deformation and failure modes: free ligament buckling, cell ligament bending, stable cell collapsing, and ligament crush induced strain hardening. The corresponding structural evolution during indentation and strain hardening were analyzed and modeled. The material scaling properties were found to be dependent on both the relative density and the secondary particle size of PUAs. Using a porosity-dependent material constitutive model, a linear relationship was found between the strain hardening index and secondary particle size instead the conventional power-law relationship. Finally, the structural efficiency of PUAs with respect to the capability for energy absorption is evaluated as a function of structural parameters and base polymeric material properties.

1. Introduction

Aerogels are highly-porous (>80%), low-density (typically <0.5 g cm^{-3}) solids with an inorganic ceramic (oxide, carbide nitride) or a polymer framework [1-3]. They were first introduced in the 1930's as a means to study the framework of sol-gel-derived wet-gels [2], and prepared by converting the pore-filling solvent of wet gels into a supercritical fluid that was vented off like a gas. In the recent years, aerogels are emerging as strong lightweight materials for applications that range from thermal insulation [4,5], to neural scaffolds [6], to environmental remediation (oil-spill clean-up) [7,8]. In most applications, high porosity is desirable but it adversely affects the mechanical properties of the

materials. A good trade-off between porosity and mechanical properties is reached when aerogels possess a bird-nest-like nanostructure of entangled fibers [4]. However, the constitutive law of such nanostructures is not well-understood or developed, rendering optimal aerogel design difficult.

With notable exceptions [5], most microstructures of polyurea (PUA) aerogels are hierarchical assemblies of elementary primary and secondary particles [30]. The nanoscopic assembly of those elementary particles depends on kinetics (monomer concentration) and solvent polarity during gelation [7]. Among various parameters of their nanostructures, the particle size, skeletal and bulk densities and their ratios can all be used to describe important features of the nanostructures. Although it does not affect the structural configurations of microstructures, they describe different perspectives of the mechanical properties of PUAs. How these parameters are related to the elastic and plastic behaviour of PUAs is addressed in this article.

Characterization of the elastic and plastic behaviour of porous materials has recently attracted significant amount of attention in research community. In macro-scale, the elastic modulus and Poisson's ratio of porous materials such as gas-injection-manufactured polymer foams with millimetre pores are usually determined from uniaxial compression experiments. However, the end frictions in this experiment often induces over-constrains. The resulting local stress variation makes the extraction of nano-scale properties of PUAs inaccurate, if not invalid [12]. To reduce the boundary effect of specimens and the requirements for surface preparation, nanoindentation has been widely used to characterize nanostructured solids [13-15]. In this case, the nonlinear tip effect must be accounted for. The elasticity, viscoelasticity, and porosity-dependent strain-

hardening law must be known in order to characterize the mechanical behaviour of nanoporous polymeric materials.

For example, the relaxation modulus extraction method [16] and the hardness interpretation approach [19] has been adopted to extract the effective elastic modulus, relaxation modulus, and the yield strength, respectively. In addition, determining the scaling properties failure mechanism of porous and cellular materials is also critical for current material system [20-30]. The scaling properties are referred to varying elastic modulus and yield strength as the relative density of the material changes. For macrocellular foams, both open- and closed-cell scaling equations were proposed by Gibson and Ashby [20] based on the mechanics of deformation on a representative cell geometry. This cell geometry was "idealized" from the results of the mechanical experiments on foams with macro pores. These equations, however, cannot be directly applied to PUAs due to the absence of any representative cell geometry and size effect [29, 30]. The effective shape coefficients need to be determined from the experimental data.

In this study, we discovered a progressive failure mechanism, which shows different responses at critical indentation depths. These critical indentation depths are associated with the varying failure mechanism. The scaling equation describing the change of effective elastic modulus with varying relative density was determined. The porosity-dependent strain hardening constitutive law was proposed and implemented to extract the hardening index. A contact mechanism was then found between secondary particles to explain the correlation between the hardening index and particle size.

2. PUA Materials

PUA wet-gels were prepared at room temperature in dry acetone from an aliphatic triisocyanate (Desmodur N3300A, courtesy of Bayer Corporation) 3× the stoichiometric amount of water and triethylamine (catalyst) as described in Eq. (1) [6]. Pore-filling acetone was extracted with liquid CO2 in an autoclave, and aerogels were obtained by taking CO2 out as a supercritical fluid. Three different formulations were considered with 11.0 g, 16.5 g and 24.0 g of Desmodur N3300A in a fixed amount of solvent (94 mL). The corresponding aerogels are referred to as PUA-11, PUA-16 and PUA-24, respectively. These three types of aerogels were selected since they provided different spatial structures, due to their different particle size and relative densities. These parameters will be linked to the mechanical properties providing the structure-property relationship for the Nanofibrous PUA materials.

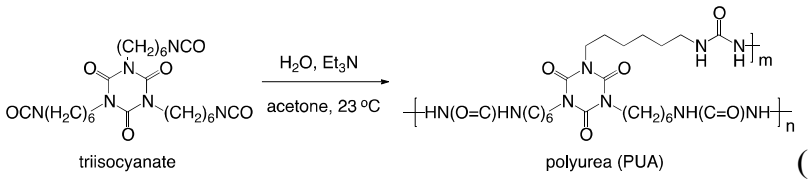

(1)

3. Research Methods

3.1 Nanostructure Characterization The bulk density ($\boldsymbol{\rho_b}$) of PUA is determined by the geometric dimensions and weight of each specimen. The skeletal density ($\boldsymbol{\rho_s}$), which is the solid density of the ligament, was determined using helium pycnometer with a Micrometrics AccuPyc II 1340 instrument. Porosities, $\boldsymbol{\Pi}$, was determined by $\boldsymbol{\Pi = 100 \times (\rho_s - \rho_b)/\rho_s}$. The particle sizes were determined using ultra-small angle and small angle neutron diffraction (USANS/SANS). More detailed information about SANS can be found in the work by Leventis et al [6]. The scanning electron microscopy (SEM) was used to image the cellular structures of

PUA. The atomic force microscopy (AFM) was used to image the deformation field after indentations.

3.2 Molecular Dynamic (MD) Modelling All atoms optimized potential for liquid simulation (OPLS- AA) is applied in our MD simulation since it was found in close agreement with the density functional theory [32-34]. For any atom type in the polyurea structure, force field parameters were chosen by matching the atom type with its corresponding atom defined in the OPLS parameter database. All MD simulations in this study are performed with LAMMPS in NVT ensemble at 300 K using the Nose–Hoover thermostat with an integration time step of 1 fs. More modelling details are listed in the supplementary information (Note1, SI).

3.3 Nanoindentation Experiments Nanoindentation was conducted using the Hysitron TI 950 TriboIndenter^{TM} equipped with a Berkovich diamond tip. Quasi-static indentations were performed on each sample under a triangular displacement over time profile with a loading/unloading rate of 1 nm/sec at various depths. At least 20 indents were performed on a freshly cleaved surface of each specimen for each depth. During each test, loading and unloading cycles were performed with holding for approximately 1 sec, and full unloading.

Elastic and Relaxation Modulus Based on the polymeric nature of the PUA, the viscoelastic and plastic behaviour were assumed. Following the approached proposed by Huang and Lu [16], Lu et al. [17], Du et al. [18]. The elastic and relaxation modulus were extracted. More extraction details are presented in the Note 2, SI.

Hardness and yield strength The hardness (H) of PUA is defined by the peak force (P) divided over the projected contact area (A_c). The yield strength (σ_y) can be linearly

related to the hardness with a coefficient (C_P). For dense bulk material, C_P is usually close to 2.5~3 due to the confinement effect from adjacent materials. For PUAs, the absence of confinement gives $C_P = 1$, which is similar as other highly porous materials such as nanoporous gold [19].

3.4 Finite element modelling Both of the extracted elastic and relaxation modulus was taken into account before PUA exceeds the yield strength. The strain-hardening phenomenon observed from force-displacement responses were also considered the finite element modelling. By treating the PUA as continuum materials, a J2-flow based plasticity model was then implemented using ABAQUS® with Subroutine UMAT. This model is based on the Desphande and Fleck's self-similar concept [23], and has a modified shape of yield surface from the conventional von Mises criterion. More details of this model are shown in Note 3, SI.

A self-similar strain hardening relationship was assumed incorporating porosity changes [23]. In the uniaxial compression setting, the post-yielding stress-strain relationship is,

$$\frac{\bar{\sigma}}{\sigma_0} = 1 + \frac{\overline{\varepsilon_p}}{\overline{\varepsilon_D}} + \gamma \ln\left[\frac{1}{1-(\overline{\varepsilon_p}/\overline{\varepsilon_D})^{\beta}}\right]. \quad (2)$$

Where σ_0 is yield strength, $\overline{\varepsilon_p}$ is the uniaxial plastic strain. Assuming the porosity change comes from the volume reduction, the relationship between the current porosity strain ($\overline{\varepsilon_D}$) and plastic strain can be obtained as, $\overline{\varepsilon_D} = \frac{f_0 - \overline{\varepsilon_p}}{1-\overline{\varepsilon_p}}$. Where γ and β are material constants, f_0 is the initial porosity of aerogels. As the stress rises, the plastic strain rises nonlinearly following an inverse power-law relationship as shown in Eq. (6).

To extract the strain-hardening properties, the parameter β is assumed to be constant as it has small impact on the shape of the strain-hardening law. The parameter γ, which

157 contributes directly to the hardening behaviour, is then obtained by fitting the
158 experimental data.

159 **4. Results and Discussion**

160 **4.1 Nanostructures** The SEM images of various PUAs are shown in Fig. 1, the overall cellular
161 structural features were observed. Based on the SANS data, the average diameters of the
162 ligament are 24, 22, and 17, respectively. The particle size difference, through small, was found
163 to contribute significantly to the strain hardening behaviour as described later in this section.

164 **4.2 Force Displacement and Depth Profile** The representative load-displacement responses are
165 presented in Fig. 2. Significant plastic deformations were observed upon fully unloading. SEM
166 images of the indentation site after different depths of indentation for PUA-11 are also shown in
167 Fig. 3a-d. The cellular nanostructure showed distinctive bending of ligaments after 500 nm of
168 indentation. However, most of the pores were slightly deformed underneath the contact surface.
169 As the indentation progresses, the pores start to collapse. We observed significant contacting and
170 crushing of the ligaments as they were pressed against each other under compression. Therefore,
171 it is suggested that prior to the 500 nm of indentation depth, most of the pores remained open
172 with ligaments slightly bent under compression. When the indentation depth approaches to 1500
173 nm, the ligaments show clear contact which gives rise to hardening behaviour. These evidences
174 indicate different stress bearing mechanisms at various indentation depths. The post-indentation
175 AFM scanning was also conducted to characterize the deformation profiles which are used to
176 calibrate the finite element modeming. More details of AFM scans are provided in the Note 4, SI.

177 **4.3 Progressive Failure Mechanism and Critical Indentation Depths** The calculated elastic
178 modulus (E_∞) and yield strengths (σ_y) at different indentation depths are presented in Fig.
179 4a-b, respectively. The results showed four stages of depth(δ)-dependent behaviour of

these properties. In stages ①, where $0 < \delta < 200$ nm, both properties increase almost linearly proportional to δ. In stage ②, where $200 < \delta < 600$ nm, the properties showed drastic drop with respect to the increase of δ. In stage ③, where $600 < \delta < 900$ nm, both the Elastic modulus and yield strength enters a short plateau at constant values. In stage ④, where $\delta > 900$ nm, the Elastic modulus show less increase for PUA-24 comparing to PUA-11 and 16. The yield strengths of all PUAs increased significantly, which are nonlinearly proportional to the increase of δ. These critical depths (200, 600, and 900 nm) are then determined to differentiate the corresponding stages as the nanostructure deforms progressively. The physics behind each stage can be explained as illustrated in Fig. 5. In the first stage, there exist independent ligaments unconnected to cells. When pressing, the independent ligaments act as end-supported columns. The low elastic modulus and yield strength could result from the buckling of these columns. As the indentation depth enters the second stage, the connected ligaments (cell structure) started to bend under compression. The excessive bending caused configurational changes to the cell structure that leads to changed effective elastic modulus and yield strengths. After the stress through ligaments exceeds the yield strengths of base materials, the cell show stable collapsing stage ③.After the deformations exceed certain level, the ligament contact initiated causing the strain hardening behavior, which gives rise to increased effective elastic modulus and yield strengths in stage ④.

4.4 Scaling Properties The average moduli of (20 indents for each sample) are 15.2, 31, and 60 MPa for PUA-11, 16, and 24, respectively. Their corresponding standard deviations are 2.1, 1.8, and 2.3 MPa. The average yield strengths obtained at stage ③ are

2.35, 4.7, and 6.36 MPa for PUA-11, 16, and 24, respectively. Their corresponding standard deviations are 0.15, 0.15, and 0.2 MPa. These yield strength values are much higher than obtained from uniaxial compression test at larger scale (with a cylindrical specimen's size of 25 mm in diameter and 50 mm in height) [21].

For porous materials, the scaling rules refer to the relationship between the relative density ratio and material properties. The backbone of this rule is that the PUA shares the same base material and structural features, which was demonstrated from MD and SANS results. According to these scaling rules, the effective elastic modulus and yield strength of general cellular solids are proportional to the powers of their relative density (bulk/skeletal) [19, 20, 21].

As shown in the SEM images (Fig. 1) of PUA with different densities, when density increases, the secondary particle size reduces leading to an increased slenderness ratio. Under compression, the bending deformation of the ligaments determines the macroscopic strains [19, 23-24]. The scaling equations for bending-dominant cellular materials have been proposed by previous studies [19, 20, 25], and can be written as,

$$\frac{E_\infty}{\mathrm{E_s}}, \frac{\sigma_\mathrm{y}}{\sigma_\mathrm{ys}} = \left(\mathrm{C_e}, \mathrm{C_y}\right)\left(\frac{\rho_\mathrm{b}}{\rho_\mathrm{s}}\right)^{(\alpha_\mathrm{e}, \alpha_\mathrm{y})} \quad (3)$$

where E_∞, σ_y are effective elastic modulus and yield strength, ρ_b is the bulk density. $\mathrm{E_s}$ and σ_ys are base material's elastic modulus and yield strength, ρ_s is the skeleton density. The proposed equations can linearly fit the mean experimental data in the logarithm plot as shown in Fig. 6. The fitting parameters are obtained as $\mathrm{C_e} = 0.87$, $\mathrm{C_y} = 1.63$, $\alpha_\mathrm{e} = 1.9$, $\alpha_\mathrm{y} = 1.8$ with the least square errors of 0.013 and 0.01. The properties of the base materials are then determined as $\mathrm{E_s} = 1.6$ GPa and $\sigma_\mathrm{ys} = 38$ MPa. From the

bending dominant deformation mechanics, α_e and α_y are 2 and 1.5 [24, 30, 37-39] respectively. These values are slightly lower than the ones obtained in this work. The difference comes from the random cell geometry. Table 2 summarizes the extracted properties and scaling parameters. These results showed significant reductions in effective elastic modulus (approximately 1/100 times of the base material modulus) and effective yield strengths (approximately 1/10 of the base material yield strength).

4.5 Porosity-dependent Strain Hardening The strain-hardening properties exhibited in stage ④ can be extracted using the finite element modelling approach described in section 3.4. More details of the finite element modeling can be found in the Note 5, SI.

The effective elastic and relaxation modulus obtained previously are used. The numerical load versus depth response are then compared with experimental data. By iteratively varying the strain hardening power index γ, the numerical results converge to the experimental values as shown in Fig. 2. It should be noted that the slight disagreement in depth range of 0-500 nm is due to the less prominent hardening effect. We also compared the AFM scanned displacement profiles of the post-indentation sites with the numerical results and found close agreement as shown in Fig. 7a. The extracted γ values for PUA-11, 16, and 24 are 7, 5, and 3. β was set to be 6 for all PUA. The normalized stress versus plastic strain response in Fig. 7b shows that PUA-11 has more rapid increase comparing to PUA-16 and 24, especially when plastic strain exceeds 0.3.

4.6 Strain Hardening and Particle Size To link the strain hardening behavior to the microstructure and deformation process. We analyzed the stress versus plastic strain response after yielding as shown in Fig. 7b. The structure enters a short stress plateau (plastic strain from 0-0.3) followed by a sharp rising part. This plateau corresponds to the structural

collapsing during compression. Beyond the plateau, the excessive bending of the ligaments causes compressive interactions among ligaments, which has been confirmed by SEM images taken after the tip retraction as shown in Fig. 8a-d. In the highly densified region under indentation, secondary particles were deformed and then compressed into each other as shown in the insert of Fig. 8e. During this process, the primary particles are pressed against each other causing densification.

As shown in Table 2, the strain hardening index γ reduces as the secondary particle size reduces. We can explain these findings use the Herzian contact theory [31]. Given the same volume and applied uniaxial force at full compaction as illustrated in Fig. 8e, we know that the contact stress ($\sigma_c = \left(\frac{F}{A}\right)/(number\ of\ contacting\ points)$) is proportional to the second order of the radius of secondary particle (R_2), i.e., $\sigma_c \propto (R_2)^2$. From Herzian contact solution [31], the contact stiffness (K) of the particle is proportional to the third order of the product of contact stress and the radius of secondary particle, i.e., $K \propto (\sigma_c R_2)^{1/3}$. Since the strain hardening index is linearly proportional to the contact stiffness K, we have $\gamma \propto K \propto R_2$, which means the strain hardening index reduces when particle size reduces. This linear relationship is demonstrated from our experiments as shown in Fig. 15e. The standard deviation away from the average strain hardening ratio ($\frac{\gamma}{R} \approx 2.233$) is about 0.05. This deviation comes from the plastic contact and physical fusion explained earlier.

4.7 Structural Efficiency Based on the scaling rules, we can identify the relationship between the increased density and increased impact resistance. The energy absorption is

defined as the area underneath the equivalent plastic strength versus plastic strain curve. The energy absorbed during the uniaxial crushing process is then,

$$W = \sigma_0 \int_0^{\varepsilon_0} \frac{\bar{\sigma}}{\sigma_0} d\left(\overline{\varepsilon_p}/\overline{\varepsilon_D}\right) = \sigma_0 \left(\varepsilon_0 + \frac{\varepsilon_0^2}{2} + \gamma(R_p) \int_0^{\varepsilon_0} \ln\left[\frac{1}{1-\left(\overline{\varepsilon_p}/\overline{\varepsilon_D}\right)^{\beta}}\right] d\left(\overline{\varepsilon_p}/\overline{\varepsilon_D}\right) \right) \quad (3)$$

Where ε_0 is the level of strain that the energy was accounted for, R_p is the secondary particle size. Based on this definition, we have two design approaches, one is to directly increase the yield strength of the base material. The second is to change the secondary particle size giving different γ. To evaluate the efficiency of both approaches, we define a structural efficiency index S_e. It is a ratio between the energy enhancements through the change of yield strength and the change of particle size, relative to PUA-11.

$$S_e = \frac{W(r_\sigma)}{W(r_p)} = \frac{r_\sigma}{r_p + \frac{\left(\varepsilon_0 + \frac{\varepsilon_0^2}{2}\right)(1-r_p)}{\gamma_0 \int_0^{\varepsilon_0} \ln\left[\frac{1}{1-\left(\overline{\varepsilon_p}/\overline{\varepsilon_D}\right)^{\beta}}\right] d\left(\overline{\varepsilon_p}/\overline{\varepsilon_D}\right) + \left(\varepsilon_0 + \frac{\varepsilon_0^2}{2}\right)}} \quad (4)$$

Where $r_\sigma = \frac{\sigma_0}{\sigma_{0,11}}$, $r_p = \frac{R_p}{R_{p,11}}$, $\sigma_{0,11}$, γ_0, $R_{p,11}$ are the yield strength, hardening index, and particle size of PUA-11. We plotted S_e with practical range of r_σ and r_p with reference plane of $S_e = 1$ in Fig. 9.

S_e can then be divided into the yielding favored zone ($S_e \geq 1$) and hardening favoured zone ($S_e < 1$). In the yielding favoured zone, the enhancement of yield strength of base materials gives higher energy absorption. In the latter, reducing hardening index (i.e., reducing particle size), gives higher energy absorption.

The S_e surfaces with $\varepsilon_0 = 0.25, \text{and } 0.75$ are also compared in Fig. 9. The two surfaces intersect at the plane of $r_p = 1$. The results show, when $r_p \geq 1$, the hardening-favored zone increases as ε_0 increases. This means it is more efficient to increase particle size to achieve higher energy absorption associated with large compressive strains. When $r_p < 1$, as ε_0 increases, the yielding-favored zone increases. It means higher efficiency of increasing yield strength to achieve higher energy absorption with large strains.

5. Conclusions

Based on particle analyses, nanoindentation, and multi-scale modelling, the following conclusions can be drawn:

(1) Primary particles were identified as the basic building elements of PUA structures that determined base material properties. A compound of approximately ten primary particles form the basis of a secondary particle.

(2) Nanofibrous PUA can be characterized by an effective unit cell as widely used in cellular structures. This feature allows a reliable prediction of crushing process of the PUA based on indentation experiments.

(3) The nonlinear response of PUA samples resulted from various deformation mechanisms of nanocellular structures. This shows the nanostructures of PUA are highly stress-sensitive, which makes PUA a potential candidate for the development of pressure sensing devices.

(4) The smaller the particle size, the less significant the strain hardening effect through particle contact and the slender the ligament between particles. Smaller particles contribute to lower effective yield strength but higher PUA porosity as desired in some

applications. Hence, controlling both particle size and ligament length independently is a future research direction to achieve the optimum properties of PUA in various applications.

(5) Due to interrelation between the secondary particle size and the base material yield strength, high energy absorption can be achieved only by taking into account their coupling effect.

Conflicts of Interest

There are no conflicts to declare.

Acknowledgements

Financial support for this study was provided by National Science Foundation under Award No. CMMI-1030399 and the ARO under Award No. W911NF-14-1-0369. We also thank Covestro LLC (formerly Bayer Corp. U.S.A.) for the generous supply of Desmodur N3300A. The authors would like to thank Professor Tengfei Jiang from Central Florida University and Professor Paul S. Ho from the University of Texas at Austin for their assistances during experiments and for their insightful discussion during the preparation of this paper.

References

1 Tyan, H.,L.; Wu, C.,Y.; Wei, K.,H. *J. Appl. Poly. Sci.* **2001**, *81*, 1742-1747.

2 Kistler S. S. *Nature* **1931**, *127*, 741-741.

3 Meador, M. A. B.; Fabrizio, E. F.; Ilhan, F.; Dass A.; Zhang, G.; Vassilaras, P.; Johnston, J. C.; Leventis, N. *Chem. Mater.* **2015**, *17*, 1085-1098.

4 Zhang, G.; Dass, A.; Rawashdeh, A.-M. M.; Thomas, J.; Counsil, J. A.; Sotiriou-Leventis, C.; Fabrizio, E. F.; Ilhan, F.; Vassilaras, P.; Scheiman, D. A.; McCorkle, L.; Palczer, A.; Johnston, J. C.; Meador, M. A. B.; Leventis, N. *J. Non-Cryst. Solids* **2004**, *350*, 152-164.

5 N. Leventis, C. Chidambareswarapattar, A. Bang, C. Sotiriou-Leventis *ACS Appl. Mater. Interfaces* **2014**, *6*, 6872-6882.]

6 Leventis, N.; Sotirious-Leventis, C.; Chandrasekaran, N.; Mulik, S.; Larimore, Z. J., Lu H.; Ghuru, Citogo.; Mang, J.T., *Chem. of Mat.*, **2010***, 22(24),* 6692-6710.

7 Zhang, G.; Rawashdeh, A.-M. M.; Sotiriou-Leventis, C.; Leventis, N. *Polymer Preprints*, **2003**, *44*, 35-36.

8 Sabri, F.; Cole, J. A.; Scarbrough, M. C.; Leventis, N. *Plos One* **2012**, *7*, 125-132.

9 Bailey, T. C.; Gatrell, A. C. Addison Wesley Longman Limited: Essex, **1995**, England

10 Tyan, H.,L.; Wu, C.,Y.; Wei, K.,H. *J. Appl. Poly. Sci.* **2001**, *81*, 1742-1747.

11 Katti, A.; Shimpi, N.; Roy, S.; Lu, H.; Fabrizio, E. F.; Dass, A.; Capadona, L. A.; Leventis, N. *Chem. Mater.* **2006**, *18*, 285-296.

12 Haj-Ali, R.: Eliasi, R.; Fourman, V.: Tzur, C.: Bar, G.; Grossman, E.; Verker, R.; Gvishi, R.; Gouzman, I.; Eliaz, N.. *Microporous and Mesoporous Materials*, **2016**, *226,* 44-52.

13 Jiang, T.; Wu, C.; Spinella L.; Im, J.; Tamura, N.; Kunz, M.; Son, H.Y.; Kim, B.G.; Huang R.; Ho P.S.. *Applied Physics Letters,* **2013**, *103*, 211906

14 Wu, C.; Huang R., Liechti, K.M. IEEE Transactions on Device and Materials Reliability, **2017**, 17(2), 1530-4388

15 Jiang. T.; Wu, C.; Im. J.; Huang R., Ho, P.S. *Journal of Microelectronics and Electronic Packaging,* **2015**, *12*, 118-122

16 Huang, G.; Lu, H., *Mech. Time-Depend Mater,* **2006***, 10,* 229-243

17 Lu, H.; Wang, B.; Ma, J.; Huang, G.; Viswanathan, H; *Time-Depend Mater,* **2003***, 7:* 189-207

18 Du, P.; Lin I-K.; Lu, H; Xin, Z.; *J. Micromech. Microeng,* **2010**, *20,* 095016

19 Hodge, A.M.; Biener, J.; Hayes, J.R.; Bythrow, P.M.; Volkert, C.A.; Hamza, A.V.. *Acta Materialia,* **2007**, *55,* 1343-1349.

20 Gibson L., Ashby M., Cambridge: Cambridge University Press, **1997**.

21 Loebs JM., *Master Thesis*, **2011**, P. 6791

22 Liu, R.; Pathak, S.; Mook, W.M.; Baldwin, J. Kevin; Mara, N.; Antoniou A.. *International Journal of Plasticity,* **2017,** *98,* 139-155

23 Deshpande V.S., Fleck N.A., *Journal of the Mechanics and Physics of Solids,* **2000**, *48,* 1253-1283

24 Gibson, L.; Ashby M., J. *Proc. R. Soc. London* **1982**, *382*, 43-69.

25 Gent, A. N.; Thomas, A. G. *J. Appl. Polym. Sci.* **1959**, *1*, 107-113.

26 Gong, L.; Kyriakides, S.; Jang, W.-Y. *Intern. J. Sol. Struct.* **2005**, *42*, 1355-1379.

27 Gong, L.; Kyriakides, S. *Intern. J. Sol. Struct.* **2004**, *42*, 1381-1399.

28 Hilyad, N. C.; Cunningham, A. *Chapman and Hall*, **1994**, *3*, 110-220.

29 Bigioni, T. P.; Lin, X., Nguyen, T. T.; Corwin, E. I.; Witten, T. A.; *Nature Mater.***2006**, *5,* 265-270.

30 Gibson, L.J., *J. R. Soc. Interface,* **2012**, *9*, 2749-2766.

31 Hertz, H. Journal Reine und Angewandte Mathmatik, **1881,** 92, 156-171.

32 Bertoldi, K. *Annu. Rev. Mater. Res.* **2017**, *47*:51–61.

33 Meza, L.R.; Das, S.; Greer, J.R. *Science*, **2014**, *345*, 1322.

34 Pal, S.; Maiti, S.; Subhash, G. *Mechanics of Materials*, **2010**, *42,* 118-133.

35 Tipton, C.R.; Han, E.; Mullin, T. *Soft Matter,* **2012***, 26,* 6880-6883.

36 Minoia, A.; Chen, L.; Beljonne, D.; Lazzaroni, R. ***2012***, *53 (24),* 5480−5490.

37 Gong, L.; Kyriakides, S.; *Int'l Journal of Solids & Structures,* **2005,** *42*, 1381–1399.

38 Gong, L.; Kyriakides, S.; *Int'l Journal of Solids & Structures,* **2005,** *42*, 1355–1379.

39 Gong, L.; Kyriakides, S.; *J. Applied Mechanics,* **2006,** *73(5)*, 807–814.

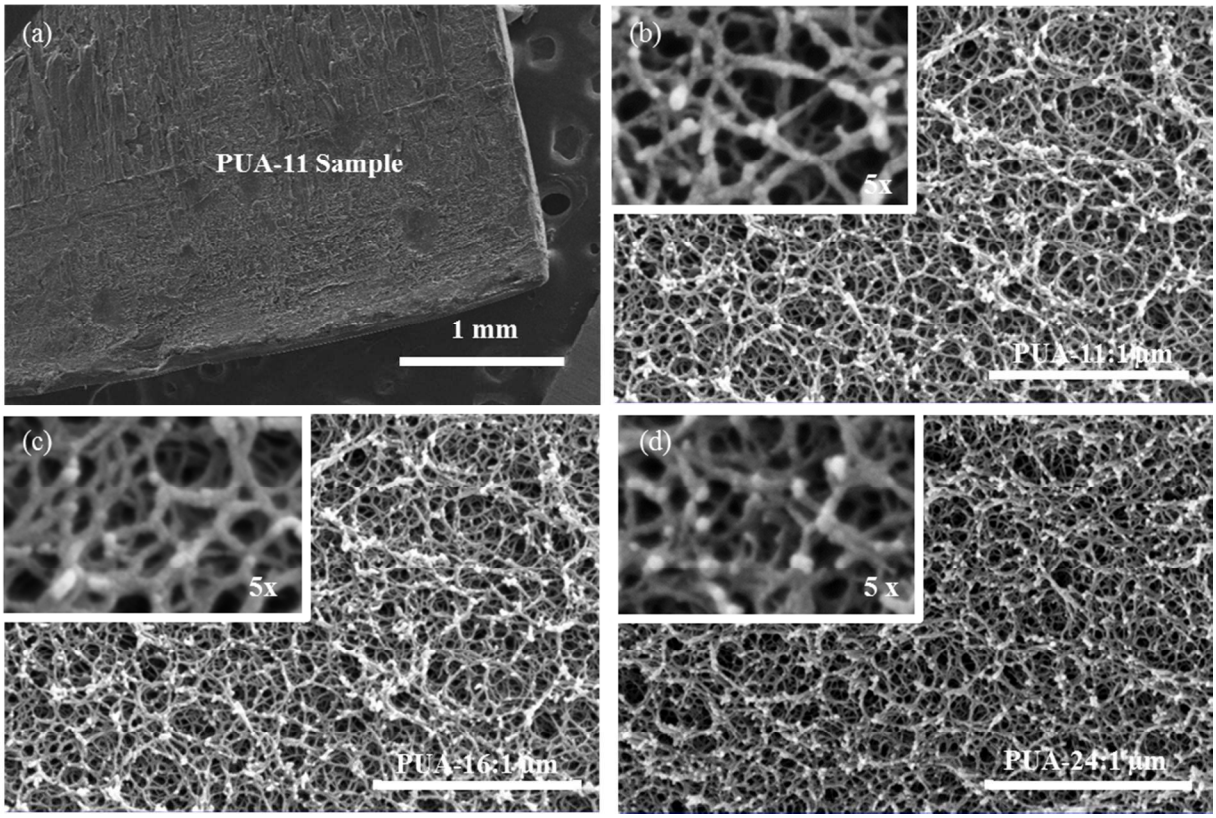

Fig. 1 SEM images showing: (a) bulk PUA-11, and nanostructures of (b) PUA-11, (c) PUA-16, (d) PUA-24. (Scale bar represents 1 μm, inserts are 5-time zoomed).

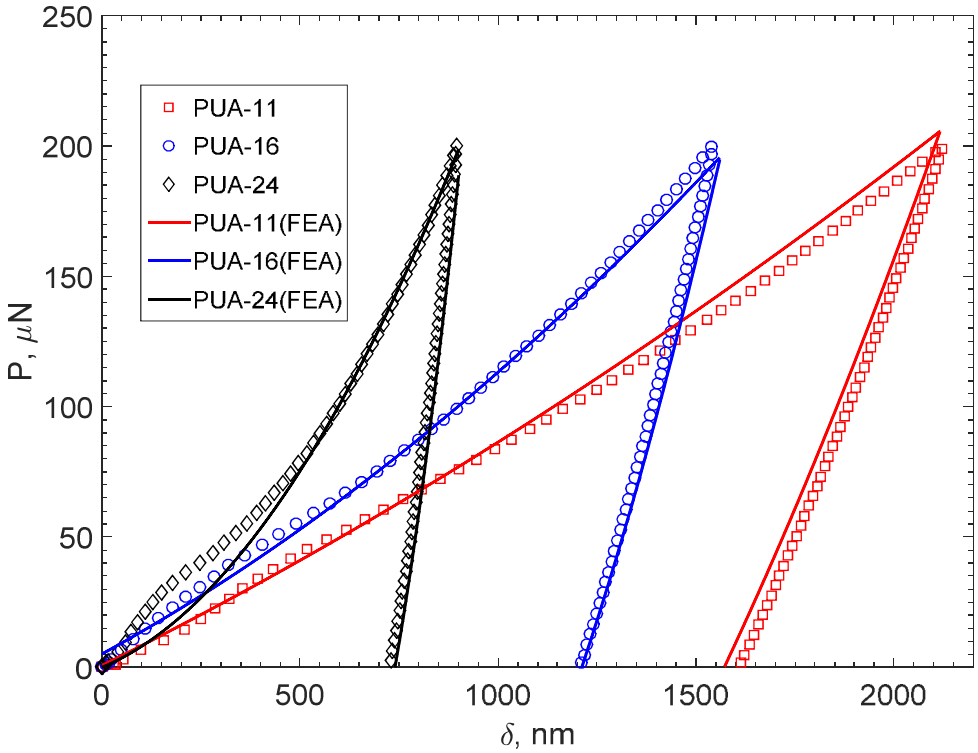

Fig. 2 Typical force displacement response

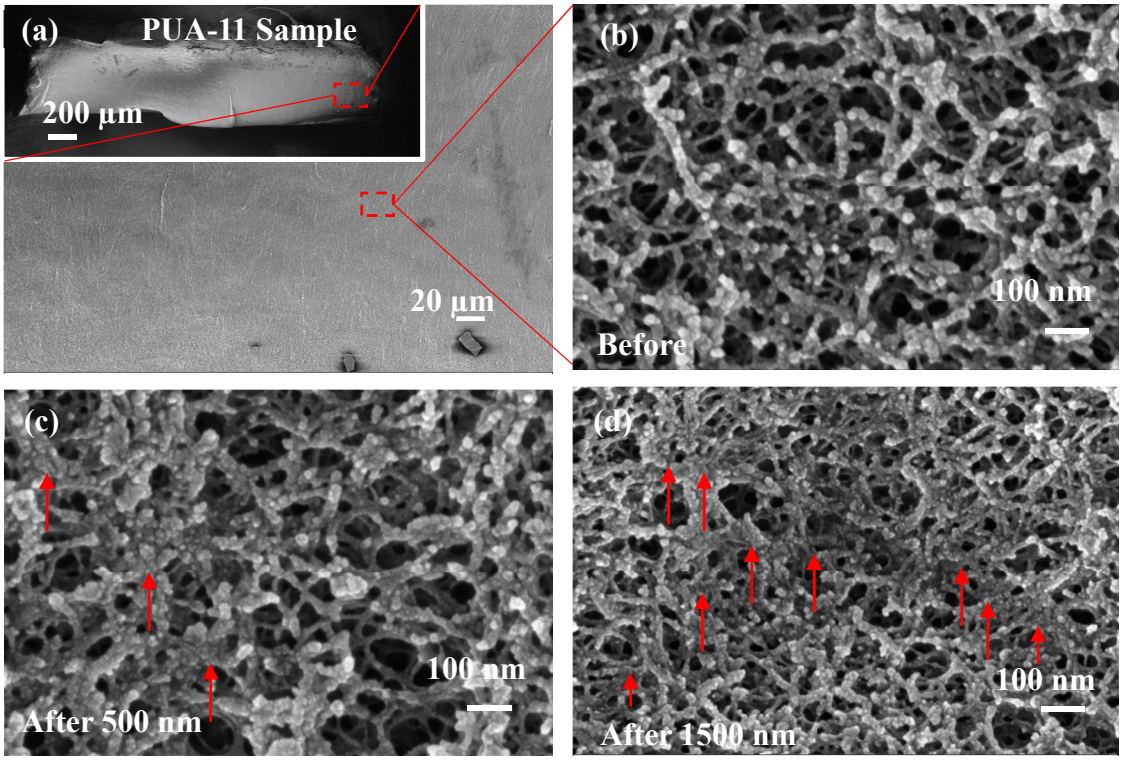

Fig. 3 Deformation progression of PUA-11 at different depths: (a) indentation location, (b) prior-to indentation, (c) after 500 nm indent and full unloading, (d) after 1500 nm indent and full unloading.

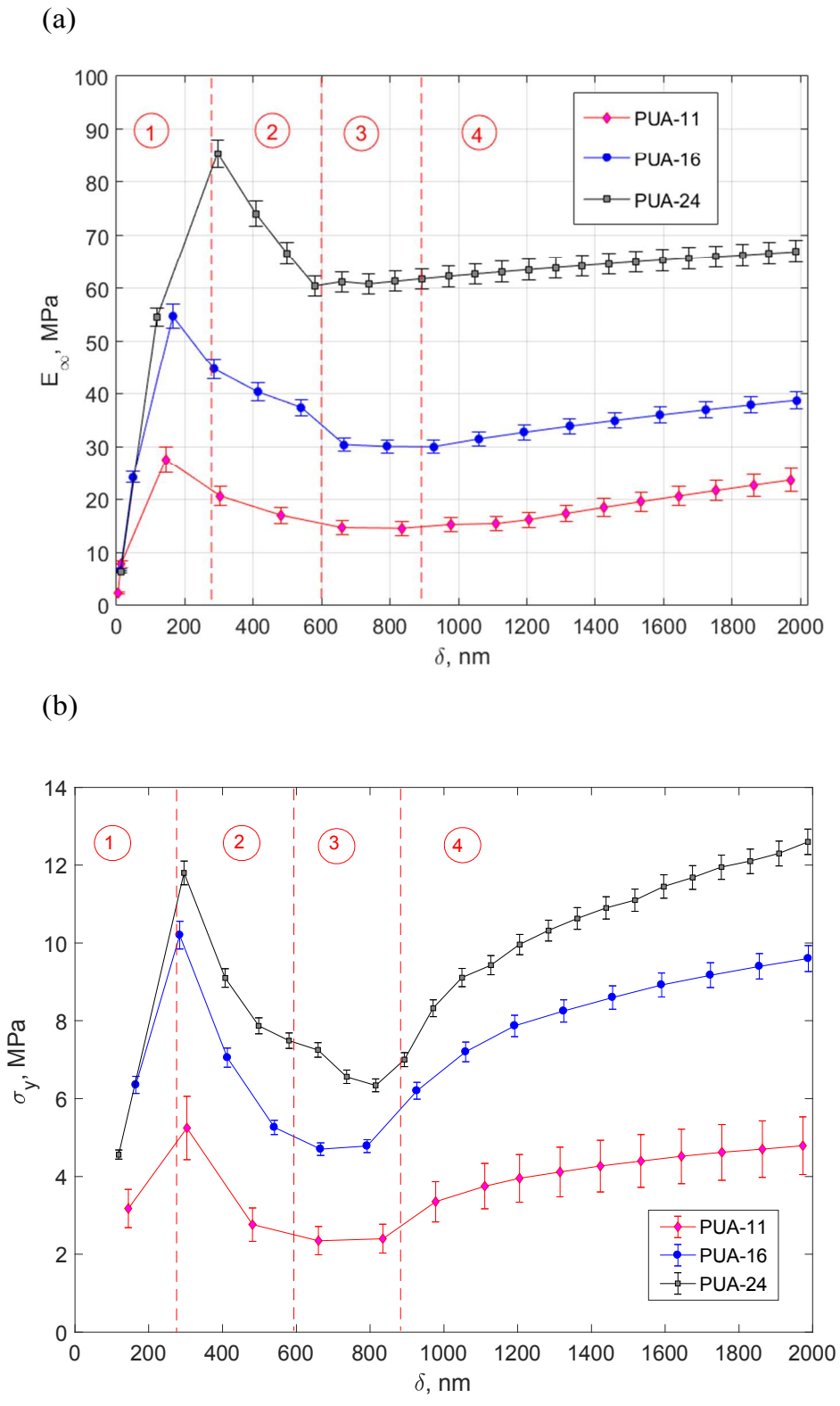

Fig. 4 (a) Elastic modulus and (b) yield strength versus indentation depth**.**

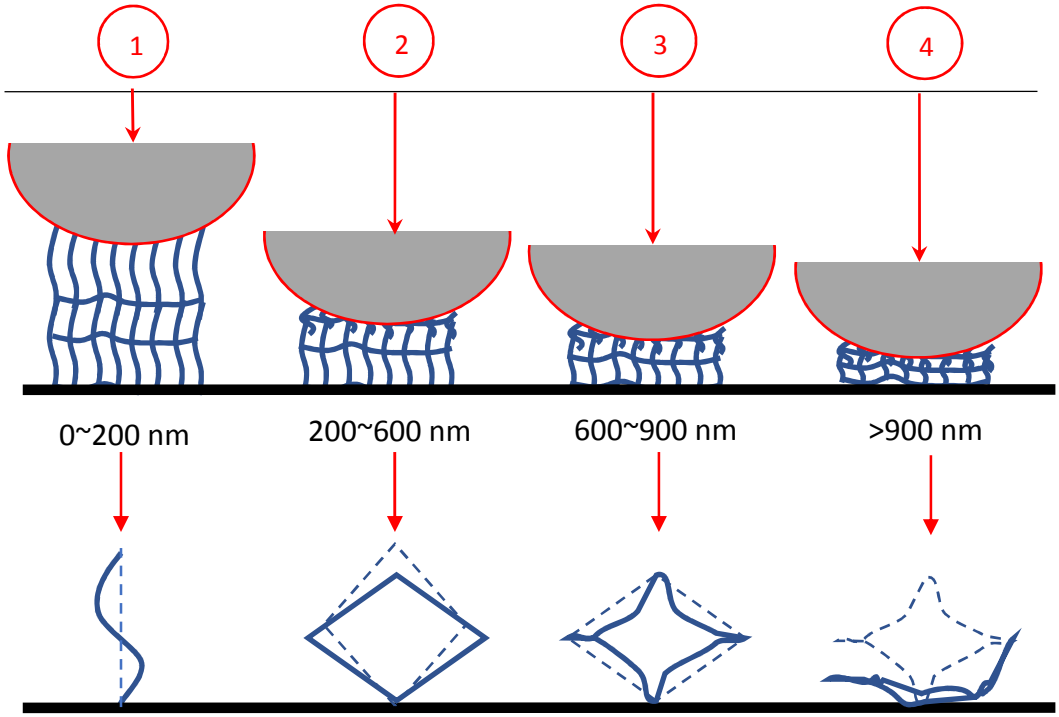

Fig. 5 Illustration of deformation stages (dashed lines show previous configuration)

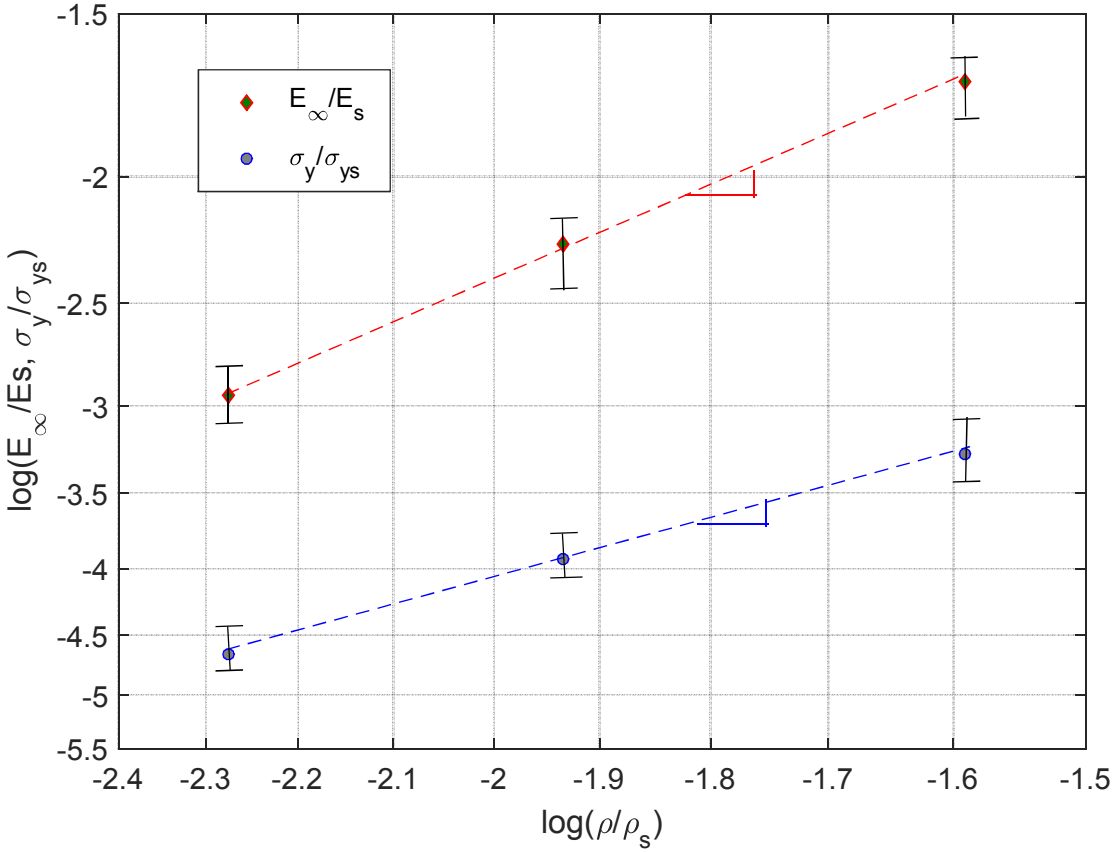

Fig. 6 Scaling properties of PUA: log-log plot of relative elastic modulus, and yield strength versus relative density.

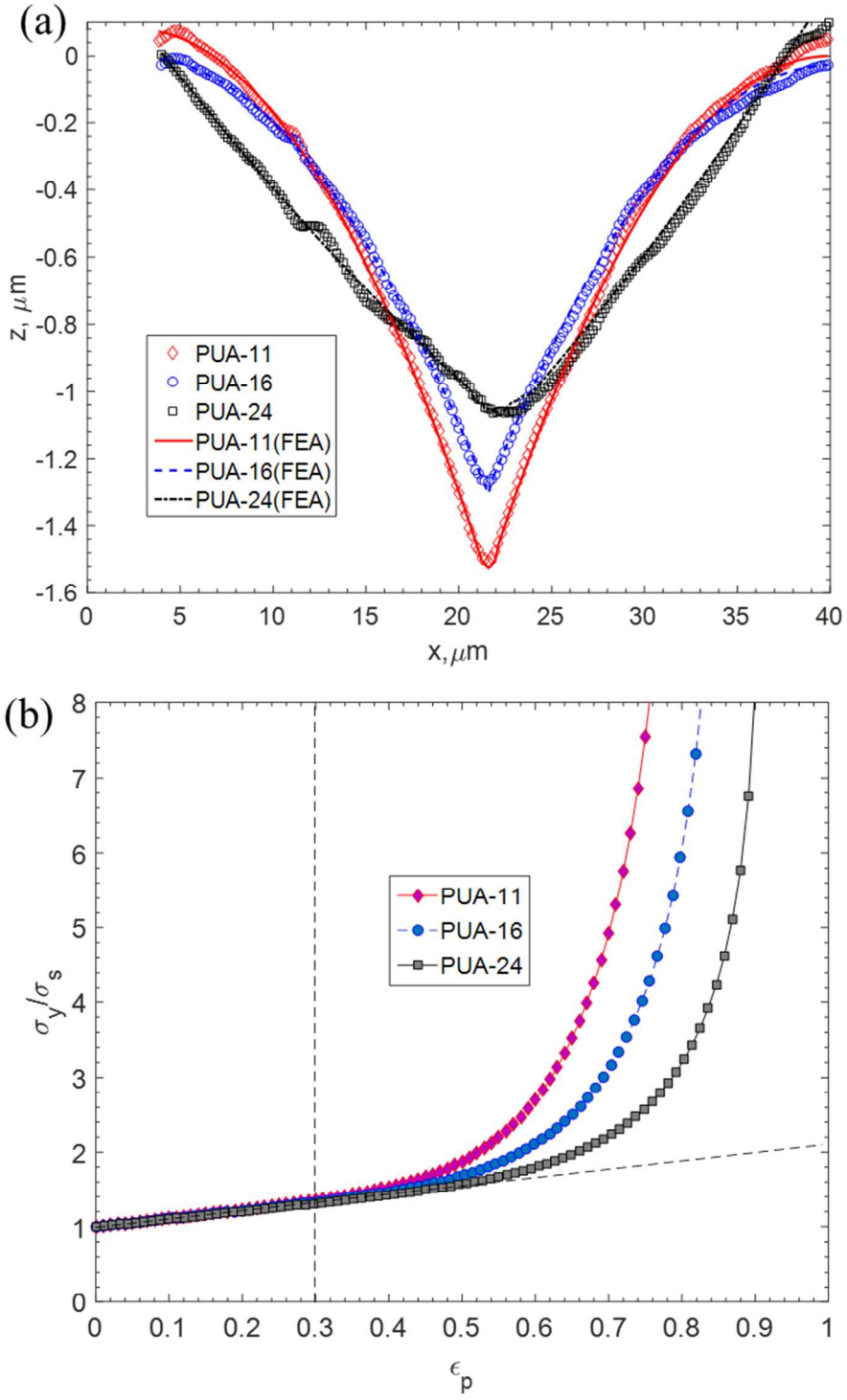

Fig. 7 Finite element modelling results: (a) deformation profiles, (b) extracted hardening relations.

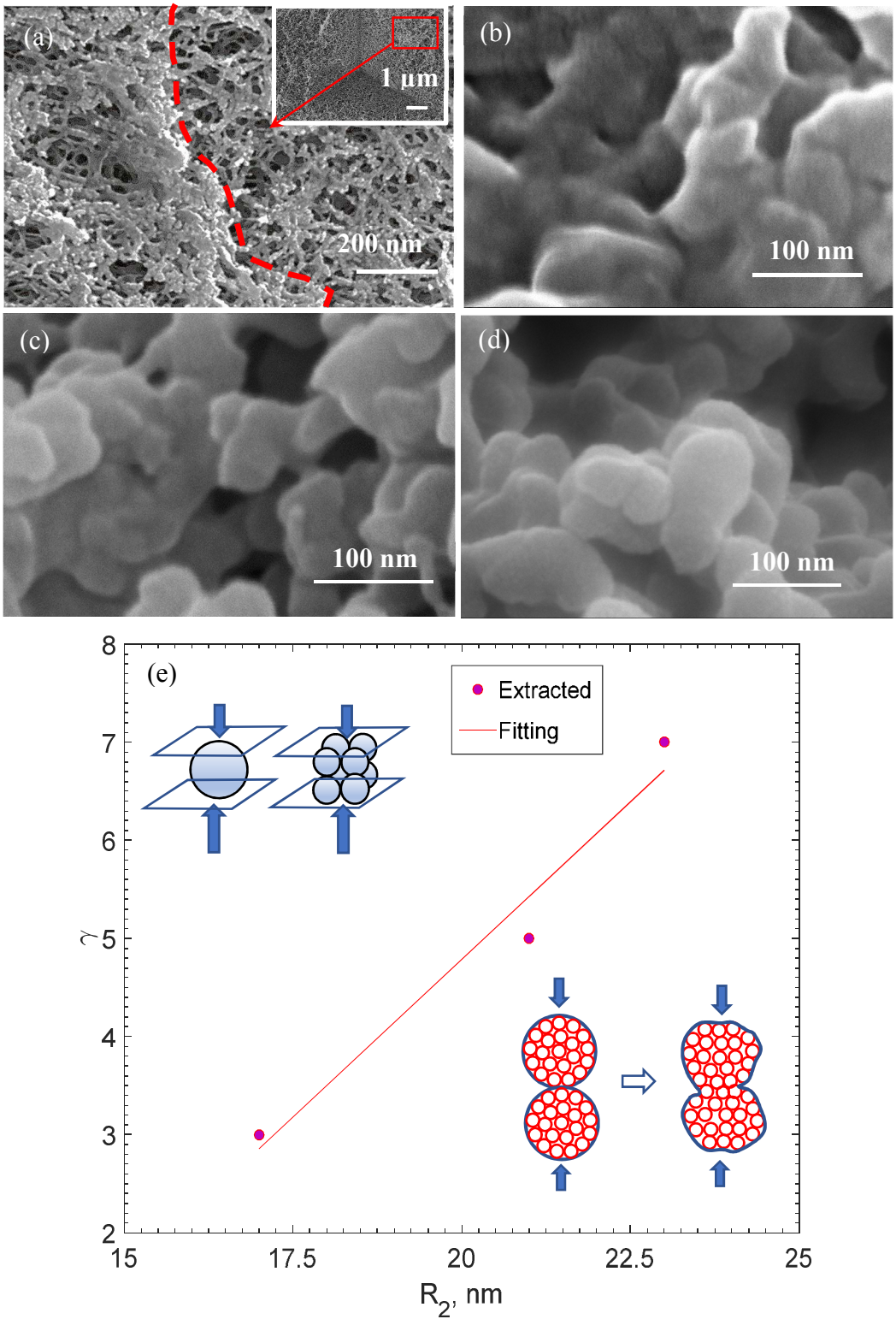

Fig. 8 Strain hardening mechanism due to contact: (a) densified nanostructures after indentation, fused particles for (b) PUA-11, (c) PUA-16, (d) PUA-24, (e) strain hardening index versus secondary particle size.

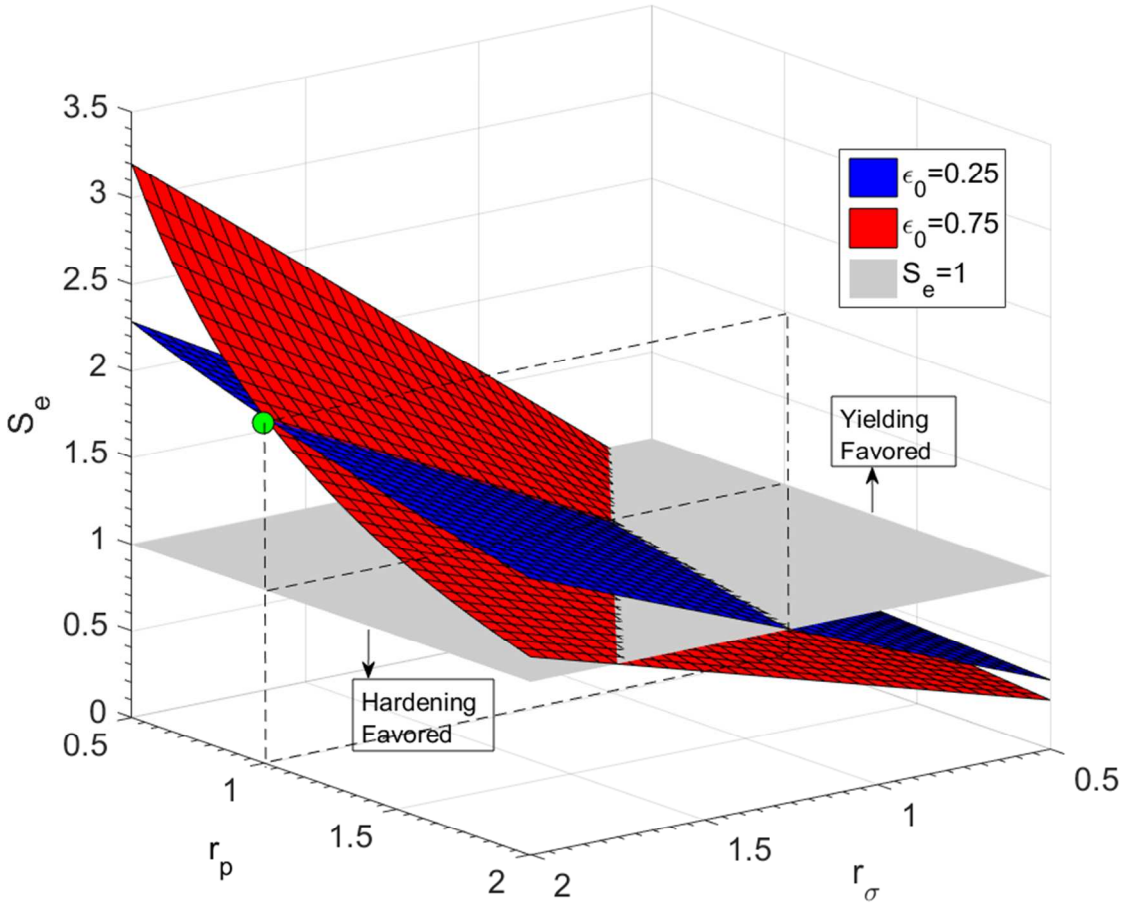

Fig. 9 Material design of PUA: structure efficiency with varying yield strength and particle size ratios.

Table 1 SANS Data of Polyurea Aerogels

Sample	ρ_b (g cm^{-3})	ρ_s (g cm^{-3})	$\prod$ (%)	R1 (nm)[a]	R2 (nm)[a]
PUA-11	0.123±0.004	1.197±0.007	89.7	7.03±0.48	23.7±0.83
PUA-16	0.173±0.002	1.199±0.002	85.5	8.09±0.47	21.9±0.1.34
PUA-24	0.244±0.016	1.200±0.002	79.7	6.8±0.30	17.0±3.92

[a]R1, R2 : radii of primary and secondary particles, respectively; Calculated from the corresponding SANS radii of gyration, RG, via R= RG/0.77.

Table 2 Scaling Properties of Polyurea Aerogels

Sample	E **(MPa)**	σ_y **(MPa)**	γ	β	E_s **(MPa)**	σ_s **(MPa)**	C_e	C_y	α_e	α_y
PUA-11	15.2±2.1	2.35±0.15	7.1	6						
PUA-16	31±1.8	4.7±0.15	5.04	6	1600	35	0.87	1.63	1.9	1.8
PUA-24	60±2.3	6.36±0.2	3.02	6						

Multi-scale Progressive Failure Mechanism and Mechanical Properties of Nanofibrous Polyurea Aerogels

Chenglin Wu,[a*], Tahereh Taghvaee [b], Congjie Wei [a], Arman Ghasemi [c], Genda Chen [a], Nicholas Leventis [b], Wei Gao [c]

[a] Department of Civil, Architectural, and Environmental Engineering, Missouri University of Science and Technology, Rolla, MO 65401,

[b] Department of Chemistry, Missouri University of Science and Technology, Rolla, MO 65401

[c] Department of Mechanical Engineering, The University of Texas at San Antonio, San Antonio, TX, 78249, United States

*Corresponding Author, Email: wuch@mst.edu

Submitted to
Soft Matter
April 2018

Research Highlights

The nonlinear mechanical properties, deformation and failure mechanisms of polyurea aerogels (PUAs) were investigated using a multi-scale approach that combines nanoindentation, analytical and computational modeling.